Finding the Sweet Spot of Photocatalysis – A Case Study using Bipyridine-based CTFs

Marcelo Alves Fávaro,[a,b]‡ Daniel Ditz,[b]‡ Jin Yang,[c] Ashta C. Ghosh,[a] Chantal Lorentz,[a] Jérôme Roeser,[c] Elsje Alessandra Quadrelli,[a] Arne Thomas,[c] Regina Palkovits,[b] Jérôme Canivet,[a]* and Florian M. Wisser[d]**

[a] Université de Lyon, Université Claude Bernard Lyon 1, CNRS, IRCELYON - UMR 5256, 2 Avenue Albert Einstein, 69626 Villeurbanne Cedex, France

[b] Institut für Technische und Makromolekulare Chemie, RWTH Aachen University, Worringerweg 2, 52074 Aachen, Germany

[c] Fakultät II Institut für Chemie, Technische Universität Berlin, Hardenbergstr. 40, 10623 Berlin, Germany

[d] Institute of Inorganic Chemistry, University of Regensburg, Universitätsstr. 31, 93053 Regensburg, Germany

KEYWORDS**:** Covalent Triazine Framework, photocatalysis, hydrogen evolution reaction, molecular control, bipyridine

ABSTRACT. Covalent Triazine Frameworks (CTFs) are a class of Porous Organic Polymers which attracts continuously growing interest because of their outstanding chemical and physical properties. However, the control of extended porous organic frameworks' structures at the molecular scale for a precise adjustment of their properties has hardly been achieved so far. Here, we present a series of bipyridine-based CTFs synthesized through polycondensation, in which the sequence of specific building blocks is well controlled. The reported synthetic strategy allows to tailor the physicochemical features of the CTF materials, including nitrogen content, apparent specific surface area and opto-electronic properties. Based on a comprehensive analytic investigation, we demonstrate a direct correlation of the CTF bipyridine content with the material features such as specific surface area, bandgap, charge separation and surface wettability with water. The entirety of those parameters dictates the catalytic activity as demonstrated for the photocatalytic hydrogen evolution reaction (HER). The material with the necessary balance between opto-electronic properties and highest hydrophilicity enables HER production rates of up to 7.2 $mmol \cdot h^{-1} \cdot g^{-1}$ under visible light irradiation and in the presence of a platinum co-catalyst.

INTRODUCTION

A current challenge in material sciences is to keep rigorous control over increasingly complex assembly of active building blocks in extended porous frameworks, while retaining predictive insight in their ultimate performance.[1] The ability to introduce various active building blocks into one porous framework has already allowed the modulation and prediction of physical and chemical properties, improving the capacity to tune fundamental properties including hydrophobicity,[2] porosity,[3,4] optical response,[5–8] and catalytic activity.[6,9–11] The capacity to extend the control over opto-electronic properties to the molecular-level, while retaining the control over other physico-chemical and structural properties, becomes key in the context of

materials applications to renewable energy utilization; the capacity to control opto-electronic properties will in turn drive the materials photocatalytic performances.

While some interesting results have been achieved in photocatalysis,[12–16] typically by adding electron acceptor (p-doping) or electron donor atoms or moieties (n-doping) in the final composition of the material,[6,13,17,18] the correlation of material's structure with the observed catalytic performance remains phenomenological,[17,19,20] as the observed changes in electronic properties, geometry and morphology seemed too intertwined to rationalize the changes in catalytic activity.[21,22]

One frontier in preparing photoactive multifunctional materials by modular design thus lies in the control and comprehension from the material's molecular structure up to the macroscopic scale, understanding material's performances in its entirety, beyond the description of its molecular units. To address these challenges, a regular, alternating assembly between building blocks containing different functional groups is a route to yield a periodic, sequential copolymer[23] with a uniform integration of the dopant.

Here, we report (*i*) a synthetic strategy for the structural control at the molecular level for a series of periodic co-polymers, namely bipyridine-containing covalent triazine frameworks (CTFs), (*ii*) a general protocol for the consistent measurement of their resulting electronic properties, e.g. frontier orbital position allignement, a feat not described yet, and (*iii*) their correlation with the obtained catalytic performances in photochemical hydrogen evolution reaction (HER) which reaches 7.2 mmol/h/g_{cat}.

RESULTS AND DISCUSSION.

Synthesis and charactrization of the materials. Four CTFs were synthesized via condensation of aromatic diamidine bromides and aromatic dialdehydes. The series of periodic co-polymers with the desired quantity and positioning of dopant in the material were adjusted

by the stoichiometric ratio of di-amidine and di-aldehyde in a 2:1 ratio for *in situ* polycondensation of the triazine linkage (**Figure 1a**). This polycondensation approach, recently reported by Cooper, Tan and co-workers,[24] provides superior control compared with the well-established ionothermal CTF synthesis,[25] paving the way to master the desired building block sequence in the bipyridine-containing CTFs family, by applying the principle of orthogonal chemistry.[26,27] However, so far, only few CTFs obtained by polycondensation are reported, mostly limited to functionalized aromatic aldehydes and non-functionalised terephthalamidine or [1,1'-biphenyl]-4,4'-bis(carboximidamide).[28–32] Here, we employed bipyridine and biphenyl aromatic cores as n-doping and non-doping moieties, respectively (**Figure 1**). Since the aromatic dialdehydes are commercially available, the synthesis of CTFs started with preparing 5,5'-diamidine-2,2'-bipyridine dihalide and 4,4'-biphenyldiamidine dihalide, adapting the previously established procedure.[24]

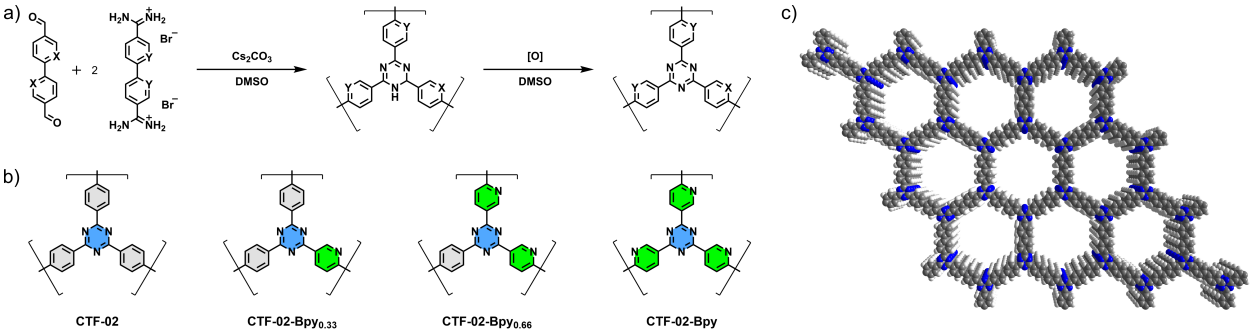

Figure 1. a) Schematic representation of triazine formation in the CTF-02 series (X, Y = CH / N) synthesized via polycondensation. **b)** Repeating units of the four different CTFs: **CTF-02** (X, Y = CH), **CTF-02-Bpy$_{0.33}$** (X = N, Y = CH), **CTF-02-Bpy$_{0.66}$** (X = CH, Y = N) and **CTF-02-Bpy** (X, Y = N). Color code: blue: triazine, green: pyridine, gray: phenyl moieties. **c)** Idealized structural model of CTF-02 stacking along the crystallographic c-direction. Color code: gray: carbon, blue: nitrogen, white: hydrogen atoms. All materials are partially ordered, characteristic for materials prepared by the polycondensation approach (**Figure S16**, **S17**).

As the synthesis of the amidine chloride produces a large excess of NH_4Cl, its purification is a crucial step. While non-functionalised terephthalamidine dichloride could be obtained in good purity following the procedure established by Shu *et al.*,[33] all attempts to obtain sufficiently

pure 5,5'-diamidine-2,2'-bipyridine by washing or recrystallisation from ethanol/acetone mixtures were unsucessful. Thus, we applied a counter ion exchange strategy to transfer the amidine first into the tetraphenylborate, which is soluble in acetone, and then into the corresponding bromide (for details see SI, section 2.1). Note that using terephthalamidine dibromide in the synthesis of **CTF-1** did not affect porosity, band-gap or crystallinity with respect to the synthesis procedure described by Cooper and co-workers applying terephthalamidine dichloride (see SI section 3).[24]

Since two molecules of amidine bromide and one of aldehyde are needed for the synthesis of a triazine core, a series of materials containing 0, 33, 66 and 100% of bipyridine building units was synthesized (**Figure 1b**). The materials were named **CTF-02**,[34] **CTF-02-Bpy$_{0.33}$**, **CTF-02-Bpy$_{0.66}$** and CTF-02-Bpy, following the increase in bipyridine content within the CTF structure. The successful co-polymerization was assessed by IR spectroscopy, elemental analysis and quantitative ^{13}C composite-pulse multiple cross polarization (ComPmultiCP) MAS NMR spectroscopy. In IR spectra, co-polymerization can be followed qualitatively, as characteristic bands of biphenyl moieties at 1416 cm^{-1} and 1000 cm^{-1} decrease in intensity when going from **CTF-02** to **CTF-02-Bpy** (**Figure S9**). At the same time, the characteristic bands of bipyridine moieties at 1467, 1050 and 1030 cm^{-1} appear.

To obtain a detailed and quantitative insight into the composition of the CTFs, ^{13}C ComPmultiCP MAS NMR spectra were recorded.[14,35,36] The signal around 170 ppm can be attributed to the triazine core carbon atom, confirming the successful condensation and oxidation of amidine and aldehydes to the triazine core in all materials (**Figure 2a**). The absence of any signal in the ^{13}C NMR spectra at about 190 ppm and 163 ppm highlights the complete transformation of aldehyde and amidine moieties in all materials (see **Figure S13**). In the spectrum of the biphenyl based material **CTF-02**, signals at 143.0, 135.1 and 128.0 ppm in an integrated ratio of 1 : 1 : 4 of the biphenyl moiety occur, while in the spectrum of **CTF-02-Bpy**,

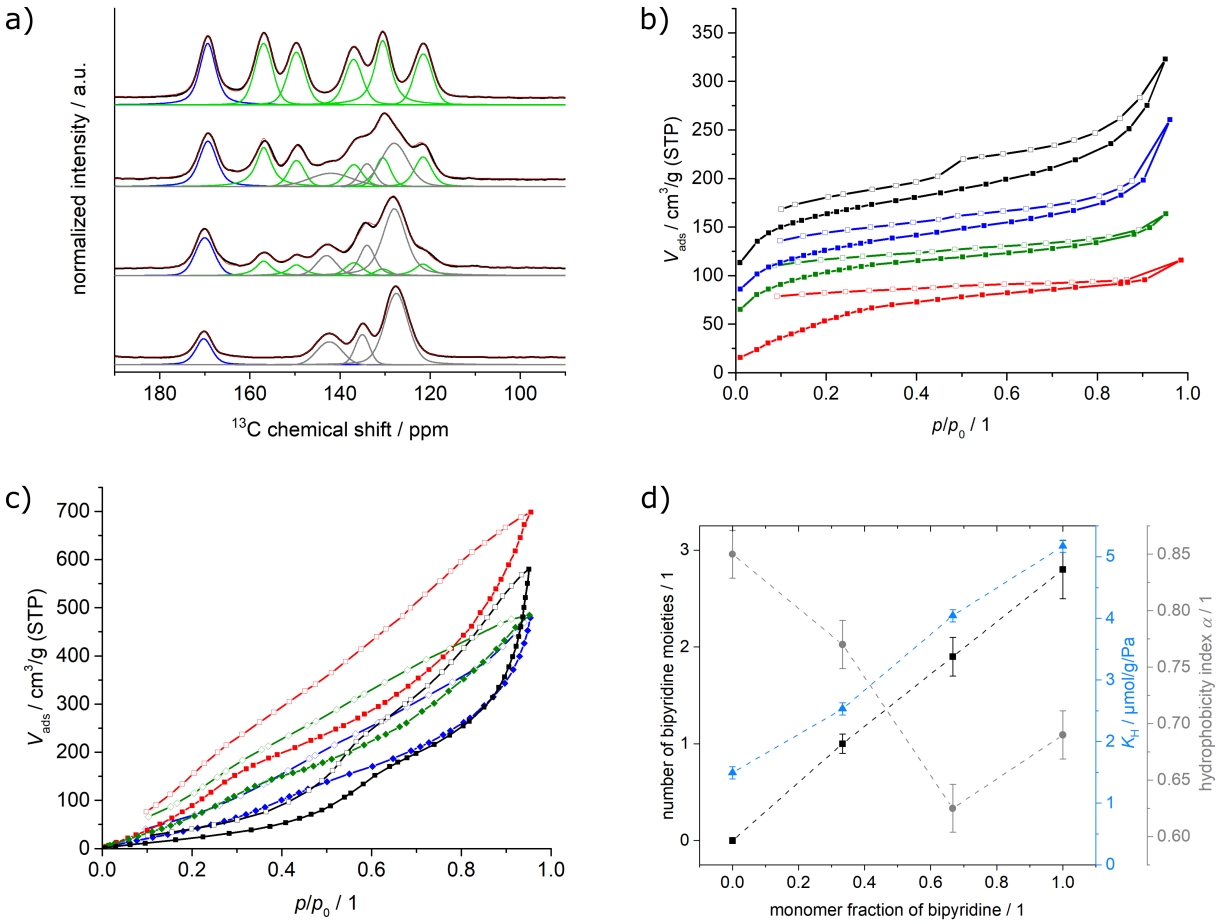

Figure 2. a) ^{13}C ComPmulti-CP MAS NMR spectra and corresponding deconvolution for **CTF-02**, **CTF-02-Bpy$_{0.33}$**, **CTF-02-Bpy$_{0.66}$** and **CTF-02-Bpy**, from bottom to top. In all spectra, a line broadening of 100 Hz was applied. Color code for deconvoluted signals: blue: triazine, green: bipyridine and gray: biphenyl carbon atoms (see also **Figure 1**). Complete NMR spectra are provided in the SI (**Figure S13**). **b)** N_2 physisorption isotherms measured at 77 K and **c)** water vapor physisorption isotherms measured at 298 K of **CTF-02** (black), **CTF-02-Bpy$_{0.33}$** (blue), **CTF-02-Bpy$_{0.66}$** (green) and **CTF-02-Bpy** (red). **d)** Experimentally observed evolution of composition from ^{13}C ComPmulti-CP MAS NMR spectroscopy (black), wettability (K_H, blue) and hydrophobicity (α, gray) as a function of monomer ratio. Dashed lines are guidelines for the eyes.

five different resonances at 156.9, 149.6, 136.9, 130.5 and 121.6 ppm appear with equal intensities (**Figure 2a**). In the spectra of the mixed CTFs, containing both biphenyl and bipyridine based monomers, all those signals are present, their integrated ratio in line with a 1-to-2 and 2-to-1 composition (see **Table 1** and SI section 4.3 for further discussion). This perfect stoichiometric control is further evidenced by elemental analysis. The nitrogen content of these materials increases linearly from 12.8% for **CTF-02** to 22.1% for **CTF-02-Bpy**, while the molar

ratio of carbon to nitrogen is in line with the theoretical composition (**Table S1**). The signal of the triazine carbon atom shifts from 170.6 ppm in **CTF-02** to 169.1 ppm in **CTF-02-Bpy$_{0.66}$** and **CTF-Bpy**. This shielding effect reflects the increase in electron density on the triazine moiety with increasing number of bipyridine ligands, reflecting the enhanced donor capability of the n-doped building block. A further increase from 66% bipyridine to 100% bipyridine did not result in a further shielding effect on the triazine moiety acting as electron acceptor.

Table 1. Monomer feed ratios and ^{13}C ComPmultiCP integrals of repeating units. Ratios are calculated from the sum of the integrals of all resonances for each repeating unit, normalized to the triazine resonance (3 carbon atoms) and divided by the number of carbon atoms per repeating unit.[36]

	monomer feed		monomer ratio from NMR	
polymer	Biphenyl	bipyridine	biphenyl	bipyridine
CTF-02	3	0	2.9 ± 0.2	0
CTF-02-Bpy$_{0.33}$	2	1	1.9 ± 0.2	1.0 ± 0.1
CTF-02-Bpy$_{0.66}$	1	2	1.0 ± 0.1	1.9 ± 0.2
CTF-02-Bpy	0	3	0	2.8 ± 0.3

All materials show a permanent porosity towards nitrogen at 77 K, together with the characteristic swelling behavior for CTFs prepared by this methodology (**Figure 2b**).[24,37] The hysteresis between absorption and desorption branch of the isotherms increases with increasing bipyridine content, indicative for a more pronounced swelling of the flexible network structure in the CTF-02-Bpy series.[38–40] The purely biphenyl-based **CTF-02** has the highest apparent surface area within the series, achieving 570 m^2/g. As for other CTFs prepared by the condensation approach,[24] the apparent surface area of **CTF-02** is significantly lower than the apparent surface areas obtained under ionothermal conditions (1880 – 2480 m^2/g),[25,34] but comparable to the apparent surface area of materials prepared by trifluoromethanesulfonic acid (TfOH) mediated polycondensation (560 m^2/g).[5,41] The observed lower surface area might be

explained by avoiding the partial carbonization that occurs during ionothermal synthesis in molten $ZnCl_2$, which may increase the surface area. The $ZnCl_2$ may also act as a porogene.[42,43] With increasing bipyridine content, and thus with increasing surface polarity (*vide infra*), the apparent surface area decreases to approx. 400, 370 and 240 m^2/g, for **CTF-02-Bpy$_{0.33}$**, **CTF-02-Bpy$_{0.66}$** and **CTF-02-Bpy**, respectively (Table 2). A possible explanation for the decrease in apparent surface area might include a non-favorable interaction of N_2 with the more polar surface of the bipyridine containing materials or a denser state of the flexible bipyridine-containing CTFs after activation and cooling to 77 K.[44]

Especially in heterogeneous catalysis, a high specific surface area in an open material is a key feature to assure accessibility of the active sites. As we aim for aqueous liquid phase catalysis, not only the apparent surface area, but also the interaction and porosity towards a given solvent has to be considered. Water vapor physisorption isotherms revealed a high water vapor uptake at high partial pressure for all materials (**Figure 2c**). The solid-solvent interaction and thus the wettability of the surface, reflected by the material's Henry constant (K_H),[45] depends on the amount of bipyridine moieties. With increasing amount of bipyridine, K_H increases linearly from $1.5 \cdot 10^{-6}$ mol/g/Pa for **CTF-02**, providing the weakest solid-solvent interaction, to $5.2 \cdot 10^{-6}$ mol/g/Pa for **CTF-02-Bpy** (Table 2, **Figure 2d**). In the same way, the degree of pore filling (Ξ),[46] increases from 0.7 to 3.1 (**Figure S14**). Thus, in all bipyridine-CTFs, the pores are completely filled with water, a beneficial characteristic for the intended application in aqueous HER. In case of **CTF-02-Bpy$_{0.66}$** and **CTF-02-Bpy**, the H_2O-accessible pore volume even strongly increased compared to N_2 accessible pore volume, highlighting the pronounced swelling of the material and therefore good accessibility of active sites even in the center of the material. An important number to evaluate the hydrophilicity is the relative partial pressure α at which the capacity for water uptake is reached to 50 %; the lower α is, the more hydrophilic

is the material.[45] In this series, the highest hydrophilicity is observed for **CTF-02-Bpy$_{0.66}$** (α = 0.63), the highest hydrophobicity for **CTF-02** (α = 0.85, **Table 2**, **Figure 2d**).

Table 2. Porosity and optical properties in the series of CTFs.

Polymer	S_{BET} / m^2/g	V_{tot} [a] / cm^3/g	V_{tot} [b] / cm^3/g	K_H / mol/g/Pa	α / 1	E_{dir} [c] / eV	E_{indir} [d] / eV
CTF-02	570	0.71	0.47	$1.5 \cdot 10^{-6}$	0.85	3.05	2.86
CTF-02-Bpy$_{0.33}$	400	0.40	0.39	$2.5 \cdot 10^{-6}$	0.77	2.98	2.73
CTF-02-Bpy$_{0.66}$	370	0.25	0.39	$4.0 \cdot 10^{-6}$	0.63	2.90	2.64
CTF-02-Bpy	240	0.18	0.56	$5.2 \cdot 10^{-6}$	0.69	2.87	2.37

[a] determined at 0.95 p/p_0 from N_2 physisorption isotherms measured at 77 K, [b] determined at 0.95 p/p_0 from H_2O vapour physisorption isotherms measured at 298 K, [c] direct and [d] indirect optical band gaps determined via the Tauc plot method (**Figure S10**).

Optical properties of the materials. The optical properties of the CTF series were investigated by diffuse reflectance UV-Vis spectroscopy (**Figure 3a**). Following the increase in the bipyridine content within the series, and consequently increased n-doping, the light absorbance shifts towards higher wavelengths, in line with predictions obtained from DFT calculations by Van Speybroeck and co-workers.[47] In the series, the direct band-gap depends on the molecular composition, *e.g.* **CTF-02** without any bipyridine moieties holds the largest direct bandgap with 3.05 eV, while **CTF-02-Bpy** possesses the narrowest direct bandgap with 2.87 eV (**Table 2**). For the indirect bandgap, a similar but more pronounced trend is observed ranging from 2.86 eV to 2.37 eV. Both the direct and indirect band gap depend linearly on the amount of bipyridine doping (**Figure S11**). However, with increasing bipyridine content a more obvious Urbach tail is visible in the Tauc plots, indicating the formation of localized or mid-band gap states from **CTF-02** to **CTF-02-Bpy** (**Figure S10**), in line with the increasing n-doping in the series.

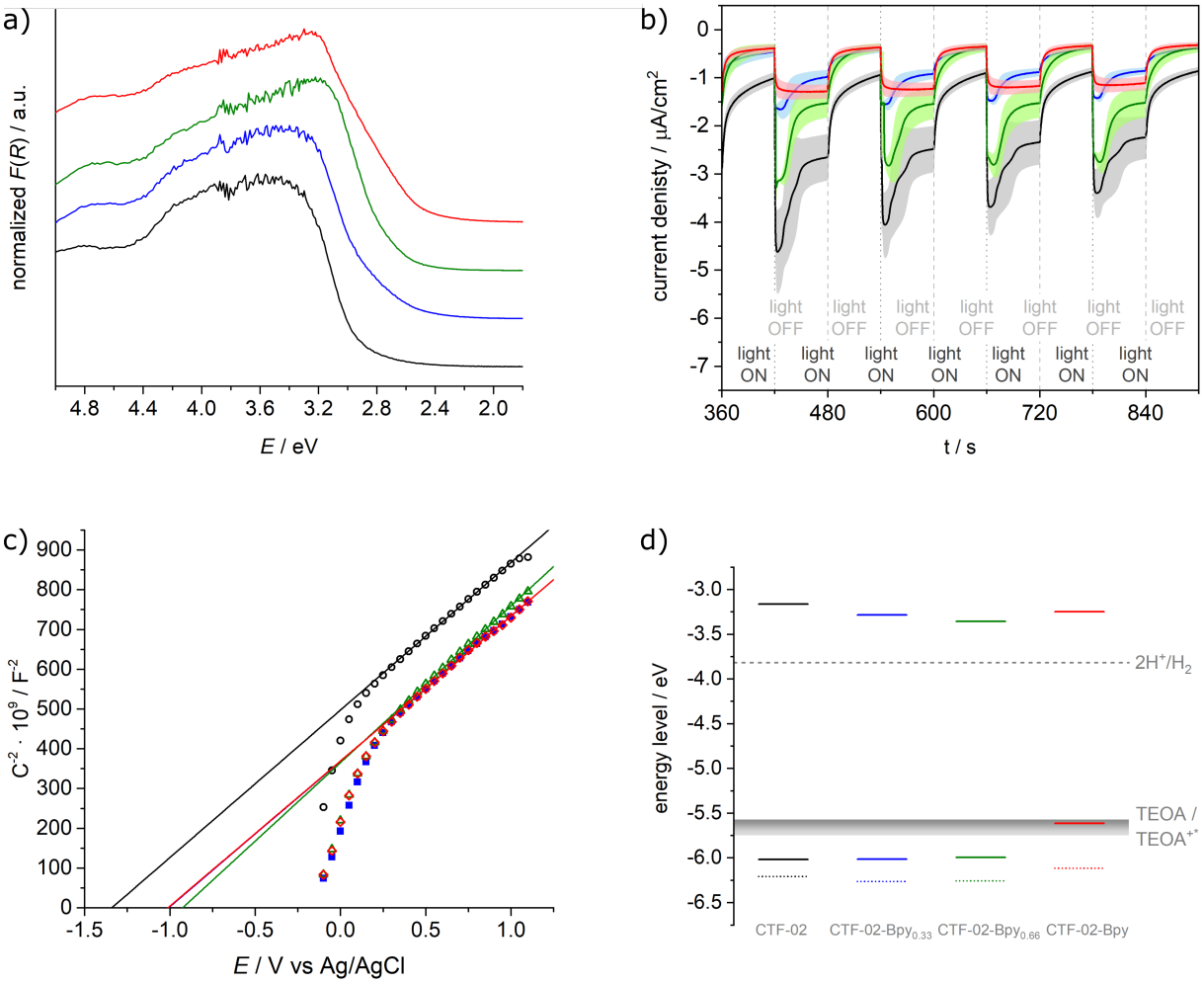

Figure 3. a) Solid-state UV Vis spectra of **CTF-02** (black), **CTF-02-Bpy$_{0.33}$** (blue), **CTF-02-Bpy$_{0.66}$** (green) and **CTF-02-Bpy** (red). **b)** Transient photocurrent measurements **CTF-02** (black), **CTF-02-Bpy$_{0.33}$** (blue), **CTF-02-Bpy$_{0.66}$** (green) and **CTF-02-Bpy** (red). The shadowed areas around each curve represent errors for several independent experiments. **c)** Mott-Schottky plot for **CTF-02** (black), **CTF-02-Bpy$_{0.33}$** (blue), **CTF-02-Bpy$_{0.66}$** (green) and **CTF-02-Bpy** (red) The data were acquired at the isoelectric point and at a potential perturbation frequency of 700 Hz (for details see SI, section 4.9). **d)** Bandgap position for CTF series and potential of proton reduction and TEOA oxidation both at pH 10.5.

Electron paramagnetic resonance (EPR) experiments in a water-triethanolamine mixture confirm the assumption of localized states. Upon illumination, the photo excited CTFs are reductively quenched by reaction with TEOA to yield the reduced CTF radical anion, highlighted by a sharp signal in the EPR spectrum at 337 mT ($g \approx 1.995 - 1.999$) characteristic for unpaired electrons on aromatic rings with most likely odd numbers of carbon atoms.[46,48–50] The EPR signal intensity increases in the same order as the Urbach tail, showing the strongest

signal intensity for **CTF-02-Bpy** (**Figure S18**). As expected, bipyridine not only brings additional electrons into the system, but also acts as a donor moiety to the triazine acceptor function, resulting in the observed increase in signal intensity and thus available unpaired electrons. Although this should reduce electron hole recombination, it does not automatically lead to a higher number of available charge carriers, as transient photocurrent measurements depict a different result (**Figure 3b**).

All CTF materials respond to light and generate a photo current under light illumination (**Figure 3b**, all samples were illuminated with 360 nm UV light in order to minimize the effect of different light absorption capability and to shift the focus to the charge transport phenomena). The negative photo-response after light illumination indicates a n-type semiconducting behavior for all materials,[51] in line with results from Mott-Schottky analyses (*vide infra*). The increased current results from a better conductivity due to additional charge carriers generated via light absorption and consequent charge separation, as already mentioned. Therefore, photocurrent measurements allow a qualitative comparison of the available charges for surface reactions. Depending on the materials' molecular composition, two different dynamic responses are observed. For the **CTF-02-Bpy** material, a fast rise within 0.6 s occurs followed by a slow rise to the steady-state current. In contrast, **CTF-02**, **CTF-02-Bpy$_{0.33}$** and **CTF-02-Bpy$_{0.66}$** are characterized by a photo response curve showing an overshoot of the response signal directly after illumination, which subsequently declines to the steady state. Such a behavior has been explained by the formation of (deeply) trapped states for which the dynamics to reach equilibrium are significantly slower than the time necessary for extraction of free charges from the active material.[52,53] Interestingly, the material with the strongest overshoot, **CTF-02** shows the longest decay time at turn-off. Such a long photocurrent tail is associated with continuous extraction of charges, even more than 10 s after turning off the illumination. In case of **CTF-02**, not all photo-generated charges are extracted from the material even after 60 s in the dark,

which may serve as a reservoir of trapped charges. Beneficial for photocatalysis, this long decay-time demonstrates that those trapped charges can be extracted from the material,[53] and should be accessible for photochemical reactions.[54–56] Thus trap-mediated recombination, which would result in a short decay-time, is not the dominating pathway over carrier extraction in these CTFs.

The measured photocurrent decreases in the order **CTF-02** > **CTF-02-Bpy$_{0.66}$** > **CTF-02-Bpy** ≈ **CTF-02-Bpy$_{0.33}$**. Although the introduction of both donor and acceptor moieties in the CTF improves charge generation, it reduces charge separation and charge transport. It has been suggested that all-carbon aromatic moieties (here biphenyl) facilitate charge separation and transfer in comparison to heteroatom-containing aromatic moieties.[57] This could explain the observed highest charge transport in **CTF-02**, but does not explain the non-monotonous order within the series of bipyridine-containing materials (**CTF-02-Bpy$_{0.66}$** > **CTF-02-Bpy** ≈ **CTF-02-Bpy$_{0.33}$**). Here, other factors must be at play to counteract the advantage of biphenyl moieties for charge separation and charge transfer. Especially the distance and the time it takes for a charge carrier to diffuse to the particle-substrate-interface, has a significant influence on the charge recombination probability. For example, a high specific surface area, porosity and wettability of the surface should shorten the average diffusion length to the interface. Since **CTF-02-Bpy$_{0.66}$** shows a greater photocurrent than **CTF-02-Bpy$_{0.33}$**, while displaying comparable apparent surface area and similar particle sizes (below 200 nm, **Figure S23**), the increased photocurrent of **CTF-02-Bpy$_{0.66}$** suggests that in this case, the positive effect of higher hydrophilicity overcomes the detrimental effect of lower biphenyl content in the overall photocurrent production. The drop of photocurrent observed when further increasing the bpy content (*viz*. increased photocurrent of **CTF-02-Bpy$_{0.66}$** with respect to **CTF-02-Bpy**) is in line with the beneficial hydrophilicity effect, which is larger for **CTF-02-Bpy$_{0.66}$** than for **CTF-02-**

Bpy; in this case, though, the adverse effect of lower biphenyl content and/or lower surface area could also concur to this drop in photocurrent (see Table 2).

Last, for the application in photocatalysis, precise knowledge of the frontier orbital positions is indispensable to assess the thermodynamic driving forces of the half-reactions; here, the proton reduction into H_2 and the oxidation of the electron donor triethanolamine (TEOA). Electrochemical impedance spectroscopy (EIS) was performed at the material-electrolyte interface, to determine the flat band potential using Mott-Schottky analyses (**Figure 3c**). The positive slope observed in the Mott-Schottky plots confirms that all material are n-type conductors. The flat band potential corresponds to the extrapolated potential for $C^{-2} = 0\ F^{-2}$, independent of the applied potential perturbation frequency. In first approximation, the flat band potential can be associated with the conduction band (CB, electron affinity) position.[58–61] Here we want to stress that prior to flat band potential measurements, knowledge of the isoelectric point (pH_{IEP}) of the material is required for rigorous determination of its flat band position.[58] This is at odds with some practices in the literature, where a pH_{IEP} close to pH 7 is assumed for CTF materials, which may cause an incorrect alignment of the frontier orbital positions of several tenths of eV, due to the neglected influence of charged surface states (see below). For example for CTF-1 a broad range of pH_{IEP} has been reported (pH 5 – 7.2).[62–65] For the bipyridine based materials, we found a pH_{IEP} around pH 4 ± 0.5, while for **CTF-02** the pH_{IEP} is at around pH 8, in line with literature data for **CTF-02** material prepared by the ionothermal method (SI, section 4.9, **Figure S20**).[63] The lowest flat band potential at pH_{IEP} in the series is achieved for **CTF-02** at approx. -3.72 eV (-1.33 V vs Ag/Ag^+), while **CTF-02-Bpy$_{0.33}$** to **CTF-02-Bpy** hold similar flat band potentials around -4.1 eV (~-0.95 V vs Ag/Ag^+). As the flat band potential is associated with the conduction band position, taking the pH dependency of the conduction band edge into account,[58] we expect the highest driving force for HER of ~650 meV for **CTF-02** and the lowest for **CTF-02-Bpy$_{0.66}$** (>460 meV, **Figure 3d**). To align the valence band (VB, minus

ionization energy) positions, we assumed that the indirect optical band gap is close to the true band gap.[59] Here, we note that the VB position is similar for **CTF-02** to **CTF-02-Bpy$_{0.66}$** and increases sharply in energy for **CTF-02-Bpy**. Thus, for all materials but **CTF-02-Bpy**, the VB position is sufficient low in energy to ensure efficient reductive quenching of the corresponding photo-excited states of the CTF by TEOA. In case of **CTF-02-Bpy**, hardly any thermodynamic driving force is observed (<<100 meV, **Figure 3d**). In addition, we note that a completely different picture will arise, if EIS was performed at pH different from pH_{IEP}, and observed differences for the VB position as large as 0.5 eV. In particular, hardly any (<<100 meV, **CTF-02-Bpy$_{0.66}$**) or even no driving force for the reductive quenching would be expected for **CTF-02-Bpy** when the EIS measurements were conducted at pH 7 or pH 10.5 (see also **Figure S21, 22**). These results highlight the importance to perform Mott Schottky analysis at the isoelectric point in order to align frontier orbitals positions precisely and to rationalize catalytic activities by calculating thermodynamic driving forces (*vide infra*).

We have seen so far that especially the ends of the series, namely **CTF-02-Bpy** and **CTF-02** possess features that should boost their performance in photocatalysis. On the one side, **CTF-02-Bpy** shows improved light absorption in the visible region and efficient charge generation, but very low thermodynamic driving force for TEOA oxidation. On the other hand, **CTF-02** possesses high thermodynamic driving forces and good visible light induced charge separation and transport,[28,37] but the highest hydrophobicity. We thus suppose that by the rational design and precise control of the material properties, we should find the material with optimum composition and thus properties, resulting in a maximum in performance of the catalysts in photocatalytic HER.

Photcatalytic HER perfomances of the materials. The series of CTFs synthesized in this work was employed as photocatalysts in sacrificial water splitting under visible light irradiation (>395 nm) using Pt as co-catalyst. The deposition of Pt is generally considered not to affect the

photophysical properties of the organic photocatalyst, but to facilitate H_2 elimination from the materials surface.[66,67]

Within the series, **CTF-02-Bpy$_{0.66}$** showed the highest activity, reaching 7.2 mmol/h/g_{cat}, while all other catalysts show activities between 3.2 and 4.7 mmol/h/g_{cat} (**Figure 4**). The trend of the HER activity cannot be pinpointed to one property alone, but rather to the sum of all optical and photo physical properties. For example, the performance of **CTF-02-Bpy** is rather low, despite its small band gap and excellent charge separation ability. This is most likely caused by the positioning of the valence band, making the reductive quenching kinetically least favored (**Figure 3d**).

Also, the rather high HER activity (4.3 mmol/h/g_{cat}) for the biphenyl-based **CTF-02** cannot be explained by its optical and photo physical properties alone. As **CTF-02** is the pure biphenyl-based polymer in the series, it possesses the weakest water wettability, as confirmed by water vapor physisorption experiments, with a degree of pore filling well below 1 (**Table 2**). Nonetheless, the high driving forces for both half reactions as well as the pronounced charge trapping observed for **CTF-02** boosts its photocatalytic activity. Overall, the properties of the interface between catalyst and reaction media (wettability, degree of pore filling, **Figure S14**) as well as charge generation improve in the series from **CTF-02** and **CTF-02-Bpy**, while the apparent surface area (**Table 2**) and the band-gap (**Figure S11**) evolve for the worse. These contrasting trends explain why they result in an optimum performance for **CTF-02-Bpy$_{0.66}$**. This optimum material composition for HER is connected, albeit not exclusively, to the materials' highest hydrophilicity in the series (**Figure 4**); the levelling off of the electron doping towards the triazine moiety at this material composition is a further indicator for its optimal composition.

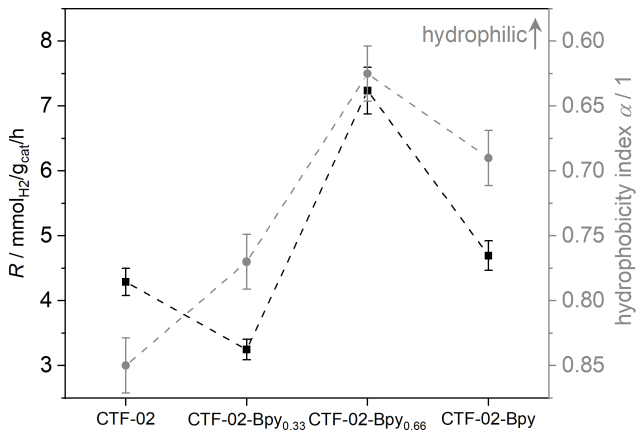

Figure 4. Overview of production rate in HER (black) and surface hydrophobicity (gray) for the four different catalysts. Dashed lines are guidelines for the eyes. HER conditions: 10 mg catalyst, 3 h, $\lambda > 395$ nm, 18 ml H_2O/TEOA (8 : 1, *V* : *V*), 5 wt% Pt.

Comparison with state of the art. Compared to other classes of porous organic polymers, like CMPs [61] and COFs,[68] the CTFs reported in this work, are among the materials with the highest activity in HER under comparable conditions, e.g. basic conditions and TEOA as sacrificial electron donor (see Table S6).[69] Comparing to the only bipyridine-containing CTF reported up to date, CTF-HUST-C6, a crystalline material synthesized from condensation between terephthalamidine chloride and 5,5'-di(hydroxymethyl)-2,2'-bipyridine, similar catalytic activities are obtained (~6.5 mmol/g_{cat}/h, Table S6, entry 10).[70] In comparison to **CTF-02** materials prepared by the TfOH-mediated polycondensation approach, we observe here an HER rate of up to one order in magnitude higher, under very similar catalytic conditions (4.3 mmol/g_{cat}/h vs. ~0.3 mmol/g_{cat}/h,[5]). The material possess similar surface areas around 570 m^2/g and bandgaps (~ 2.8 eV).[5] We note however, that a direct comparison between different materials, even with very similar structure as in the case of the **CTF-02** materials, is complex, as not only the band-gap and surface area affect the catalytic activity. As demonstrated above, in particular the precise positioning of the absolute frontier orbitals, the dynamics of photo response and the solvent-solid interactions (wettability, hydrophilicity) have a marked influence on a material's performance, and yet these parameters are scarcely reported

CONCLUSION.

In summary, we have demonstrated that, by using polycondensation reaction, it is possible to systematically change the molecular composition of covalent triazine-based frameworks. The sequence of the molecular building blocks, and thus the level of doping of the pristine CTF with electron-rich bipyridine moieties (n-doping), correlate directly with the material features such as specific surface area, bandgap and surface wettability with water, which are crucial for the photocatalytic activity of the CTFs in hydrogen evolution reaction. In the series, we showed that doping CTFs with bipyridine moieties results in an increase in the solvent-solid interactions and in more efficient charge separation, beneficial for HER reaction. In contrast, it results also in reduced bandgap and surface, potentially detrimental to the HER reaction. Altogether, those properties drastically influence the photocatalytic activity thus leading to a sweet spot in HER activity with 66% of bipyridine building units in the framework. This local maximum was both anticipated based on physico-chemical properties of the material and experimentally observed.

By carefully adjusting those properties, the best material, **CTF-02-Bpy$_{0.66}$**, reaches the highest hydrogen evolution rate, achieving 7.24 mmol h^{-1} g^{-1} under visible light irradiation in the presence of a sacrificial compound. Importantly, these investigations show that the balance between all properties that might affect (photo)catalytic activity is crucial to accurately describe the materials performance and to understand the parameter that affects most its performance. The unprecedented control over the building block sequence at a molecular level allows for the modulation of chemical, optoelectronic, and textural properties in CTFs and thus opens a new avenue into the design and synthesis of highly performing materials.

ASSOCIATED CONTENT

Supporting Information. Detailed experimental procedures, materials and instruments used as well as addition material characterization and overview are provided in the Supporting Information.

AUTHOR INFORMATION

Corresponding Author

E-mail: florian.wisser@ur.de

E-mail: jerome.canivet@ircelyon.univ-lyon1.fr

E-mail: palkovits@itmc.rwth-aachen.de

Author Contributions

The manuscript was written through contributions of all authors. All authors have given approval to the final version of the manuscript. ‡These authors contributed equally.

ACKNOWLEDGMENT

M.A.-F., J.C, E.A.Q. and R.P. gratefully thank the SINCHEM Joint Doctorate program selected under the Erasmus Mundus Action 1 Program (FPA 2013-0037). M.A.-F and R.P acknowledge the Fuel Science Center (EXC 3782186, ID: 390919832) funded by the Excellence Initiative by the German federal and state governments. D.D. gratefully thanks the German Federal Environmental Foundation for financial support (grant number: 20019/629-32). F.M.W. gratefully acknowledges financial support from the Deutsche Forschungsgemeinschaft (DFG, grant number WI 4721/1-1 and WI 4721/3-1) and from CNRS through Momentum 2018 excellence grant (F.M.W. and A.C.G). A.T. and J.R. acknowledge the BMBF (Bundesministerium für Bildung und Forschung) for funding through the project PRODIGY

(CO2WIN, 033RC024A). We would also like to thank Amitava Acharjya for his help during the photocatalytic experiments and Ulrike Schießl for recording SEM images.

REFERENCES

(1) Hassan, Z.; Matt, Y.; Begum, S.; Tsotsalas, M.; Bräse, S. Assembly of Molecular Building Blocks into Integrated Complex Functional Molecular Systems: Structuring Matter Made to Order. *Adv. Funct. Mater.* **2020**, *30* (26), 1907625. https://doi.org/10.1002/adfm.201907625.

(2) Iemhoff, A.; Deischter, J.; Jung, S.; Tuci, G.; Giambastiani, G.; Palkovits, R. Polymer-Inspired Covalent Triazine Frameworks from the Carbonaceous Side – Influence of Unexpected Surface Functionalisation on Liquid-Phase Adsorption Processes. *J. Mater. Chem. A* **2021**, *9* (9), 5390–5403. https://doi.org/10.1039/D0TA10195H.

(3) Kim, B.; Park, N.; Lee, S. M.; Kim, H. J.; Son, S. U. Insights into the Low Surface Area of Conjugated Microporous Polymers and Methodological Suggestion for the Enhancement of Porosity. *Polym. Chem.* **2015**, *6* (42), 7363–7367. https://doi.org/10.1039/C5PY01141H.

(4) Mollart, C.; Trewin, A. Rationalising the Influence of Solvent Choice on the Porosity of Conjugated Microporous Polymers. *Phys. Chem. Chem. Phys.* **2020**, *22* (38), 21642–21645. https://doi.org/10.1039/D0CP03539D.

(5) Meier, C. B.; Sprick, R. S.; Monti, A.; Guiglion, P.; Lee, J.-S. M.; Zwijnenburg, M. A.; Cooper, A. I. Structure-Property Relationships for Covalent Triazine-Based Frameworks: The Effect of Spacer Length on Photocatalytic Hydrogen Evolution from Water. *Polymer (Guildf).* **2017**, *126*, 283–290. https://doi.org/10.1016/j.polymer.2017.04.017.

(6) Sprick, R. S.; Jiang, J.; Bonillo, B.; Ren, S.; Ratvijitvech, T.; Guiglion, P.; Zwijnenburg, M. A.; Adams, D. J.; Cooper, A. I. Tunable Organic Photocatalysts for Visible-Light-Driven

Hydrogen Evolution. *J. Am. Chem. Soc.* **2015**, *137* (9), 3265–3270. https://doi.org/10.1021/ja511552k.

(7) Kochergin, Y. S.; Schwarz, D.; Acharjya, A.; Ichangi, A.; Kulkarni, R.; Eliášová, P.; Vacek, J.; Schmidt, J.; Thomas, A.; Bojdys, M. J. Exploring the "Goldilocks Zone" of Semiconducting Polymer Photocatalysts by Donor-Acceptor Interactions. *Angew. Chemie Int. Ed.* **2018**, *57* (43), 14188–14192. https://doi.org/10.1002/anie.201809702.

(8) Schwarz, D.; Acharja, A.; Ichangi, A.; Lyu, P.; Opanasenko, M. V.; Goßler, F. R.; König, T. A. F.; Čejka, J.; Nachtigall, P.; Thomas, A.; Bojdys, M. J. Fluorescent Sulphur- and Nitrogen-Containing Porous Polymers with Tuneable Donor–Acceptor Domains for Light-Driven Hydrogen Evolution. *Chem. – A Eur. J.* **2018**, *24* (46), 11916–11921. https://doi.org/10.1002/chem.201802902.

(9) Beine, A. K.; Krüger, A. J. D.; Artz, J.; Weidenthaler, C.; Glotzbach, C.; Hausoul, P. J. C.; Palkovits, R. Selective Production of Glycols from Xylitol over Ru on Covalent Triazine Frameworks – Suppressing Decarbonylation Reactions. *Green Chem.* **2018**, *20* (6), 1316–1322. https://doi.org/10.1039/C8GC00208H.

(10) Tuci, G.; Pilaski, M.; Ba, H.; Rossin, A.; Luconi, L.; Caporali, S.; Pham-Huu, C.; Palkovits, R.; Giambastiani, G. Unraveling Surface Basicity and Bulk Morphology Relationship on Covalent Triazine Frameworks with Unique Catalytic and Gas Adsorption Properties. *Adv. Funct. Mater.* **2017**, *27* (7), 1605672. https://doi.org/10.1002/adfm.201605672.

(11) Wisser, F. M.; Berruyer, P.; Cardenas, L.; Mohr, Y.; Quadrelli, E. A.; Lesage, A.; Farrusseng, D.; Canivet, J. Hammett Parameter in Microporous Solids as Macroligands for

Heterogenized Photocatalysts. *ACS Catal.* **2018**, *8* (3), 1653–1661. https://doi.org/10.1021/acscatal.7b03998.

(12) Chakraborty, J.; Nath, I.; Song, S.; Mohamed, S.; Khan, A.; Heynderickx, P. M.; Verpoort, F. Porous Organic Polymer Composites as Surging Catalysts for Visible-Light-Driven Chemical Transformations and Pollutant Degradation. *J. Photochem. Photobiol. C Photochem. Rev.* **2019**, *41*, 100319. https://doi.org/10.1016/j.jphotochemrev.2019.100319.

(13) Lee, J. M.; Cooper, A. I. Advances in Conjugated Microporous Polymers. *Chem. Rev.* **2020**, *120* (4), 2171–2214. https://doi.org/10.1021/acs.chemrev.9b00399.

(14) Wisser, F. M.; Duguet, M.; Perrinet, Q.; Ghosh, A. C.; Alves-Favaro, M.; Mohr, Y.; Lorentz, C.; Quadrelli, E. A.; Palkovits, R.; Farrusseng, D.; Mellot-Draznieks, C.; Waele, V.; Canivet, J. Molecular Porous Photosystems Tailored for Long-Term Photocatalytic CO 2 Reduction. *Angew. Chemie Int. Ed.* **2020**, *59* (13), 5116–5122. https://doi.org/10.1002/anie.201912883.

(15) Chaoui, N.; Trunk, M.; Dawson, R.; Schmidt, J.; Thomas, A. Trends and Challenges for Microporous Polymers. *Chem. Soc. Rev.* **2017**, *46* (11), 3302–3321. https://doi.org/10.1039/C7CS00071E.

(16) Banerjee, T.; Gottschling, K.; Savasci, G.; Ochsenfeld, C.; Lotsch, B. V. H 2 Evolution with Covalent Organic Framework Photocatalysts. *ACS Energy Lett.* **2018**, *3* (2), 400–409. https://doi.org/10.1021/acsenergylett.7b01123.

(17) Wang, Y.; Vogel, A.; Sachs, M.; Sprick, R. S.; Wilbraham, L.; Moniz, S. J. A.; Godin, R.; Zwijnenburg, M. A.; Durrant, J. R.; Cooper, A. I.; Tang, J. Current Understanding and Challenges of Solar-Driven Hydrogen Generation Using Polymeric Photocatalysts. *Nat. Energy* **2019**, *4* (9), 746–760. https://doi.org/10.1038/s41560-019-0456-5.

(18) Li, L.; Fang, W.; Zhang, P.; Bi, J.; He, Y.; Wang, J.; Su, W. Sulfur-Doped Covalent Triazine-Based Frameworks for Enhanced Photocatalytic Hydrogen Evolution from Water under Visible Light. *J. Mater. Chem. A* **2016**, *4* (32), 12402–12406. https://doi.org/10.1039/C6TA04711D.

(19) Sachs, M.; Sprick, R. S.; Pearce, D.; Hillman, S. A. J.; Monti, A.; Guilbert, A. A. Y.; Brownbill, N. J.; Dimitrov, S.; Shi, X.; Blanc, F.; Zwijnenburg, M. A.; Nelson, J.; Durrant, J. R.; Cooper, A. I. Understanding Structure-Activity Relationships in Linear Polymer Photocatalysts for Hydrogen Evolution. *Nat. Commun.* **2018**, *9* (1), 4968. https://doi.org/10.1038/s41467-018-07420-6.

(20) Zhang, G.; Lan, Z.-A.; Wang, X. Conjugated Polymers: Catalysts for Photocatalytic Hydrogen Evolution. *Angew. Chemie Int. Ed.* **2016**, *55* (51), 15712–15727. https://doi.org/10.1002/anie.201607375.

(21) Vyas, V. S.; Haase, F.; Stegbauer, L.; Savasci, G.; Podjaski, F.; Ochsenfeld, C.; Lotsch, B. V. A Tunable Azine Covalent Organic Framework Platform for Visible Light-Induced Hydrogen Generation. *Nat. Commun.* **2015**, *6* (1), 8508. https://doi.org/10.1038/ncomms9508.

(22) Haase, F.; Banerjee, T.; Savasci, G.; Ochsenfeld, C.; Lotsch, B. V. Structure–Property–Activity Relationships in a Pyridine Containing Azine-Linked Covalent Organic Framework for Photocatalytic Hydrogen Evolution. *Faraday Discuss.* **2017**, *201*, 247–264. https://doi.org/10.1039/C7FD00051K.

(23) Jenkins, A.; Kratochvil, P.; Stepto, R.; Suter, U. International , Union of Pure Glossary of Basic Terms in Polymer. *Pure Appl. Chem.* **1996**, *68* (12), 2287–2311.

(24) Wang, K.; Yang, L.-M.; Wang, X.; Guo, L.; Cheng, G.; Zhang, C.; Jin, S.; Tan, B.; Cooper, A. Covalent Triazine Frameworks via a Low-Temperature Polycondensation

Approach. *Angew. Chemie Int. Ed.* **2017**, *56* (45), 14149–14153. https://doi.org/10.1002/anie.201708548.

(25) Kuhn, P.; Antonietti, M.; Thomas, A. Porous, Covalent Triazine-Based Frameworks Prepared by Ionothermal Synthesis. *Angew. Chemie Int. Ed.* **2008**, *47* (18), 3450–3453. https://doi.org/10.1002/anie.200705710.

(26) Liu, S.; Dicker, K. T.; Jia, X. Modular and Orthogonal Synthesis of Hybrid Polymers and Networks. *Chem. Commun.* **2015**, *51* (25), 5218–5237. https://doi.org/10.1039/C4CC09568E.

(27) Li, Z.-L.; Li, Z.-C. Periodic Copolymers by Step-Growth Polymerization. In *Sequence-Controlled Polymers*; Lutz, J.-F., Ed.; Wiley-VCH Verlag GmbH & Co. KGaA: Weinheim, Germany, Germany, 2017; pp 349–377. https://doi.org/10.1002/9783527806096.ch12.

(28) Guo, L.; Niu, Y.; Xu, H.; Li, Q.; Razzaque, S.; Huang, Q.; Jin, S.; Tan, B. Engineering Heteroatoms with Atomic Precision in Donor–Acceptor Covalent Triazine Frameworks to Boost Photocatalytic Hydrogen Production. *J. Mater. Chem. A* **2018**, *6* (40), 19775–19781. https://doi.org/10.1039/C8TA07391K.

(29) Jiang, Y.; Oh, I.; Joo, S. H.; Buyukcakir, O.; Chen, X.; Lee, S. H.; Huang, M.; Seong, W. K.; Kim, J. H.; Rohde, J.-U.; Kwak, S. K.; Yoo, J.-W.; Ruoff, R. S. Organic Radical-Linked Covalent Triazine Framework with Paramagnetic Behavior. *ACS Nano* **2019**, *13* (5), 5251–5258. https://doi.org/10.1021/acsnano.8b09634.

(30) Liao, L.; Ditz, D.; Zeng, F.; Alves Favaro, M.; Iemhoff, A.; Gupta, K.; Hartmann, H.; Szczuka, C.; Jakes, P.; Hausoul, P. J. C.; Artz, J.; Palkovits, R. Efficient Photocatalytic Oxidation of Aromatic Alcohols over Thiophene-based Covalent Triazine Frameworks with A

Narrow Band Gap. *ChemistrySelect* **2020**, *5* (45), 14438–14446. https://doi.org/10.1002/slct.202004115.

(31) Hao, W.; Chen, R.; Zhang, Y.; Wang, Y.; Zhao, Y. Triazine-Based Conjugated Microporous Polymers for Efficient Hydrogen Production. *ACS Omega* **2021**, *6* (37), 23782–23787. https://doi.org/10.1021/acsomega.1c02592.

(32) Guo, L.; Wang, X.; Zhan, Z.; Zhao, Y.; Chen, L.; Liu, T.; Tan, B.; Jin, S. Crystallization of Covalent Triazine Frameworks via a Heterogeneous Nucleation Approach for Efficient Photocatalytic Applications. *Chem. Mater.* **2021**, *33* (6), 1994–2003. https://doi.org/10.1021/acs.chemmater.0c03716.

(33) Shu, Y.; Lei, H.; Tan, Y. N.; Meng, M.; Zhang, X. C.; Liu, C. Y. Tuning the Electronic Coupling in Mo 2 –Mo 2 Systems by Variation of the Coordinating Atoms of the Bridging Ligands. *Dalt. Trans.* **2014**, *43* (39), 14756–14765. https://doi.org/10.1039/C4DT00786G.

(34) Osadchii, D. Y.; Olivos-Suarez, A. I.; Bavykina, A. V.; Gascon, J. Revisiting Nitrogen Species in Covalent Triazine Frameworks. *Langmuir* **2017**, *33* (50), 14278–14285. https://doi.org/10.1021/acs.langmuir.7b02929.

(35) Johnson, R. L.; Schmidt-Rohr, K. Quantitative Solid-State 13C NMR with Signal Enhancement by Multiple Cross Polarization. *J. Magn. Reson.* **2014**, *239*, 44–49. https://doi.org/10.1016/j.jmr.2013.11.009.

(36) Brownbill, N. J.; Sprick, R. S.; Bonillo, B.; Pawsey, S.; Aussenac, F.; Fielding, A. J.; Cooper, A. I.; Blanc, F. Structural Elucidation of Amorphous Photocatalytic Polymers from Dynamic Nuclear Polarization Enhanced Solid State NMR. *Macromolecules* **2018**, *51* (8), 3088–3096. https://doi.org/10.1021/acs.macromol.7b02544.

(37) Zhang, S.; Cheng, G.; Guo, L.; Wang, N.; Tan, B.; Jin, S. Strong-Base-Assisted Synthesis of a Crystalline Covalent Triazine Framework with High Hydrophilicity via Benzylamine Monomer for Photocatalytic Water Splitting. *Angew. Chemie Int. Ed.* **2020**, *59* (15), 6007–6014. https://doi.org/10.1002/anie.201914424.

(38) Tsyurupa, M. P.; Davankov, V. A. Porous Structure of Hypercrosslinked Polystyrene: State-of-the-Art Mini-Review. *React. Funct. Polym.* **2006**, *66* (7), 768–779. https://doi.org/10.1016/j.reactfunctpolym.2005.11.004.

(39) Ghanem, B. S.; Msayib, K. J.; McKeown, N. B.; Harris, K. D. M.; Pan, Z.; Budd, P. M.; Butler, A.; Selbie, J.; Book, D.; Walton, A. A Triptycene-Based Polymer of Intrinsic Microposity That Displays Enhanced Surface Area and Hydrogen Adsorption. *Chem. Commun.* **2007**, No. 1, 67–69. https://doi.org/10.1039/B614214A.

(40) Rose, M.; Böhlmann, W.; Sabo, M.; Kaskel, S. Element–Organic Frameworks with High Permanent Porosity. *Chem. Commun.* **2008**, No. 21, 2462. https://doi.org/10.1039/b718925g.

(41) Sun, T.; Liang, Y.; Xu, Y. Rapid, Ordered Polymerization of Crystalline Semiconducting Covalent Triazine Frameworks. *Angew. Chemie Int. Ed.* **2021**. https://doi.org/10.1002/anie.202113926.

(42) Artz, J. Covalent Triazine-Based Frameworks-Tailor-Made Catalysts and Catalyst Supports for Molecular and Nanoparticulate Species. *ChemCatChem* **2018**, *10* (8), 1753–1771. https://doi.org/10.1002/cctc.201701820.

(43) Qian, Z.; Wang, Z. J.; Zhang, K. A. I. Covalent Triazine Frameworks as Emerging Heterogeneous Photocatalysts. *Chem. Mater.* **2021**, *33* (6), 1909–1926. https://doi.org/10.1021/acs.chemmater.0c04348.

(44) Troschke, E.; Nguyen, K. D.; Paasch, S.; Schmidt, J.; Nickerl, G.; Senkovska, I.; Brunner, E.; Kaskel, S. Integration of an N-Heterocyclic Carbene Precursor into a Covalent Triazine Framework for Organocatalysis. *Chem. - A Eur. J.* **2018**, *24* (70), 18629–18633. https://doi.org/10.1002/chem.201804373.

(45) Canivet, J.; Bonnefoy, J.; Daniel, C.; Legrand, A.; Coasne, B.; Farrusseng, D. Structure–Property Relationships of Water Adsorption in Metal–Organic Frameworks. *New J. Chem.* **2014**, *38* (7), 3102–3111. https://doi.org/10.1039/C4NJ00076E.

(46) Wisser, F. M.; Eckhardt, K.; Wisser, D.; Böhlmann, W.; Grothe, J.; Brunner, E.; Kaskel, S. Tailoring Pore Structure and Properties of Functionalized Porous Polymers by Cyclotrimerization. *Macromolecules* **2014**, *47* (13), 4210–4216. https://doi.org/10.1021/ma500512j.

(47) De Vos, A.; Lejaeghere, K.; Muniz Miranda, F.; Stevens, C. V.; Van Der Voort, P.; Van Speybroeck, V. Electronic Properties of Heterogenized Ru(<scp>ii</Scp>) Polypyridyl Photoredox Complexes on Covalent Triazine Frameworks. *J. Mater. Chem. A* **2019**, *7* (14), 8433–8442. https://doi.org/10.1039/C9TA00573K.

(48) Tabbal, M.; Christidis, T.; Isber, S.; Mérel, P.; El Khakani, M. A.; Chaker, M.; Amassian, A.; Martinu, L. Correlation between the Sp2-Phase Nanostructure and the Physical Properties of Unhydrogenated Carbon Nitride. *J. Appl. Phys.* **2005**, *98* (4), 044310. https://doi.org/10.1063/1.2009817.

(49) Li, C.; Zhou, T.; Yan, M.; Cheng, S.; Wang, Y.; Sun, J.; Chen, G.; Dong, H. Intramolecular π-Conjugated Channel Expansion Achieved by Doping Cross-Linked Dopants into Carbon Nitride Frameworks for Propelling Photocatalytic Hydrogen Evolution and Mechanism Insight. *Inorg. Chem. Front.* **2021**. https://doi.org/10.1039/D1QI01122G.

(50) Li, H.; Lee, H.-Y.; Park, G.-S.; Lee, B.-J.; Park, J.-D.; Shin, C.-H.; Hou, W.; Yu, J.-S. Conjugated Polyene-Functionalized Graphitic Carbon Nitride with Enhanced Photocatalytic Water-Splitting Efficiency. *Carbon N. Y.* **2018**, *129*, 637–645. https://doi.org/10.1016/j.carbon.2017.12.048.

(51) Guo, L.; Wang, X. Q.; Zheng, X. T.; Yang, X. L.; Xu, F. J.; Tang, N.; Lu, L. W.; Ge, W. K.; Shen, B.; Dmowski, L. H.; Suski, T. Revealing of the Transition from N- to p-Type Conduction of InN:Mg by Photoconductivity Effect Measurement. *Sci. Rep.* **2015**, *4* (1), 4371. https://doi.org/10.1038/srep04371.

(52) McNeill, C. R.; Hwang, I.; Greenham, N. C. Photocurrent Transients in All-Polymer Solar Cells: Trapping and Detrapping Effects. *J. Appl. Phys.* **2009**, *106* (2), 024507. https://doi.org/10.1063/1.3177337.

(53) Gao, F.; Li, Z.; Wang, J.; Rao, A.; Howard, I. A.; Abrusci, A.; Massip, S.; McNeill, C. R.; Greenham, N. C. Trap-Induced Losses in Hybrid Photovoltaics. *ACS Nano* **2014**, *8* (4), 3213–3221. https://doi.org/10.1021/nn501185h.

(54) Xu, H. Q.; Hu, J.; Wang, D.; Li, Z.; Zhang, Q.; Luo, Y.; Yu, S. H.; Jiang, H. L. Visible-Light Photoreduction of CO2 in a Metal-Organic Framework: Boosting Electron-Hole Separation via Electron Trap States. *J. Am. Chem. Soc.* **2015**, *137* (42), 13440–13443. https://doi.org/10.1021/jacs.5b08773.

(55) Kasap, H.; Caputo, C. A.; Martindale, B. C. M.; Godin, R.; Lau, V. W.; Lotsch, B. V.; Durrant, J. R.; Reisner, E. Solar-Driven Reduction of Aqueous Protons Coupled to Selective Alcohol Oxidation with a Carbon Nitride–Molecular Ni Catalyst System. *J. Am. Chem. Soc.* **2016**, *138* (29), 9183–9192. https://doi.org/10.1021/jacs.6b04325.

(56) Vattikuti, S. V. P.; Reddy, P. A. K.; Shim, J.; Byon, C. Visible-Light-Driven Photocatalytic Activity of SnO 2 –ZnO Quantum Dots Anchored on g-C 3 N 4 Nanosheets for Photocatalytic Pollutant Degradation and H 2 Production. *ACS Omega* **2018**, *3* (7), 7587–7602. https://doi.org/10.1021/acsomega.8b00471.

(57) Zhang, J.; Zhang, G.; Chen, X.; Lin, S.; Möhlmann, L.; Dołęga, G.; Lipner, G.; Antonietti, M.; Blechert, S.; Wang, X. Co-Monomer Control of Carbon Nitride Semiconductors to Optimize Hydrogen Evolution with Visible Light. *Angew. Chemie Int. Ed.* **2012**, *51* (13), 3183–3187. https://doi.org/10.1002/anie.201106656.

(58) Beranek, R. (Photo)Electrochemical Methods for the Determination of the Band Edge Positions of TiO 2 -Based Nanomaterials. *Adv. Phys. Chem.* **2011**, *2011* (Iv), 1–20. https://doi.org/10.1155/2011/786759.

(59) Xie, J.; Shevlin, S. A.; Ruan, Q.; Moniz, S. J. A.; Liu, Y.; Liu, X.; Li, Y.; Lau, C. C.; Guo, Z. X.; Tang, J. Efficient Visible Light-Driven Water Oxidation and Proton Reduction by an Ordered Covalent Triazine-Based Framework. *Energy Environ. Sci.* **2018**, *11* (6), 1617–1624. https://doi.org/10.1039/C7EE02981K.

(60) Chen, J.; Tao, X.; Li, C.; Ma, Y.; Tao, L.; Zheng, D.; Zhu, J.; Li, H.; Li, R.; Yang, Q. Synthesis of Bipyridine-Based Covalent Organic Frameworks for Visible-Light-Driven Photocatalytic Water Oxidation. *Appl. Catal. B Environ.* **2020**, *262* (September 2019), 118271. https://doi.org/10.1016/j.apcatb.2019.118271.

(61) Bai, Y.; Wilbraham, L.; Slater, B. J.; Zwijnenburg, M. A.; Sprick, R. S.; Cooper, A. I. Accelerated Discovery of Organic Polymer Photocatalysts for Hydrogen Evolution from Water through the Integration of Experiment and Theory. *J. Am. Chem. Soc.* **2019**, *141* (22), 9063–9071. https://doi.org/10.1021/jacs.9b03591.

(62) Liu, J.; Zong, E.; Fu, H.; Zheng, S.; Xu, Z.; Zhu, D. Adsorption of Aromatic Compounds on Porous Covalent Triazine-Based Framework. *J. Colloid Interface Sci.* **2012**, *372* (1), 99–107. https://doi.org/10.1016/j.jcis.2012.01.011.

(63) An, F.; Liu, J.; Xu, Z.; Zheng, S. Efficient Removal of Three Dyes Using Porous Covalent Triazine Frameworks: Adsorption Mechanism and Role of Pore Distribution. *Water Sci. Technol.* **2020**, *82* (12), 3023–3031. https://doi.org/10.2166/wst.2020.550.

(64) Li, L.; Li, X.; Cheng, Z.; Bi, J.; Liang, S.; Zhang, Z.; Yu, Y.; Wu, L. Rapid Water Disinfection over a Ag/AgBr/Covalent Triazine-Based Framework Composite under Visible Light. *Dalt. Trans.* **2018**, *47* (20), 7077–7082. https://doi.org/10.1039/C8DT01070F.

(65) Yin, C.; Zhang, Z.; Zhou, J.; Wang, Y. Single-Layered Nanosheets of Covalent Triazine Frameworks (CTFs) by Mild Oxidation for Molecular-Sieving Membranes. *ACS Appl. Mater. Interfaces* **2020**, *12* (16), 18944–18951. https://doi.org/10.1021/acsami.0c03246.

(66) Wang, X.; Maeda, K.; Thomas, A.; Takanabe, K.; Xin, G.; Carlsson, J. M.; Domen, K.; Antonietti, M. A Metal-Free Polymeric Photocatalyst for Hydrogen Production from Water under Visible Light. *Nat. Mater.* **2009**, *8* (1), 76–80. https://doi.org/10.1038/nmat2317.

(67) Bi, S.; Yang, C.; Zhang, W.; Xu, J.; Liu, L.; Wu, D.; Wang, X.; Han, Y.; Liang, Q.; Zhang, F. Two-Dimensional Semiconducting Covalent Organic Frameworks via Condensation at Arylmethyl Carbon Atoms. *Nat. Commun.* **2019**, *10* (1), 2467. https://doi.org/10.1038/s41467-019-10504-6.

(68) Sheng, J.; Dong, H.; Meng, X.; Tang, H.; Yao, Y.; Liu, D.; Bai, L.; Zhang, F.; Wei, J.; Sun, X. Effect of Different Functional Groups on Photocatalytic Hydrogen Evolution in Covalent-Organic Frameworks. *ChemCatChem* **2019**, *11* (9), 2313–2319. https://doi.org/10.1002/cctc.201900058.

(69) Wu, S.; Pan, Y.; Lin, H.; Li, L.; Fu, X.; Long, J. Crystalline Covalent Organic Frameworks with Tailored Linkages for Photocatalytic H 2 Evolution. *ChemSusChem* **2021**, *14* (22), 4958–4972. https://doi.org/10.1002/cssc.202101625.

(70) Liu, M.; Huang, Q.; Wang, S.; Li, Z.; Li, B.; Jin, S.; Tan, B. Crystalline Covalent Triazine Frameworks by In Situ Oxidation of Alcohols to Aldehyde Monomers. *Angew. Chemie Int. Ed.* **2018**, *57* (37), 11968–11972. https://doi.org/10.1002/anie.201806664.